

Title: Emergence of electric-field-tunable interfacial ferromagnetism in 2D antiferromagnet heterostructures

Authors: Guanghui Cheng^{1,2,3,12}, Mohammad Mushfiquur Rahman⁴, Zhiping He⁵, Andres Llacahuanga Alcca^{2,3,6}, Avinash Rustagi⁴, Kirstine Aggerbeck Stampe⁷, Yanglin Zhu⁸, Shaohua Yan⁹, Shangjie Tian⁹, Zhiqiang Mao⁸, Hechang Lei⁹, Kenji Watanabe¹⁰, Takashi Taniguchi¹¹, Pramey Upadhyaya^{3,4,6}, Yong P. Chen^{1,2,3,4,6,7*}

Affiliations:

¹WPI-AIMR International Research Center for Materials Sciences, Tohoku University, Sendai 980-8577, Japan.

²Department of Physics and Astronomy, and Birck Nanotechnology Center, Purdue University, West Lafayette, Indiana 47907, USA.

³Purdue Quantum Science and Engineering Institute, Purdue University, West Lafayette, Indiana 47907, USA.

⁴School of Electrical and Computer Engineering, Purdue University, West Lafayette, Indiana 47907, USA.

⁵Department of Physics, University of Science and Technology of China, Hefei, Anhui 230026, China.

⁶Quantum Science Center, Oak Ridge, Tennessee 37831 USA.

⁷Institute of Physics and Astronomy and Villum Centers for Dirac Materials and for Hybrid Quantum Materials, Aarhus University, 8000 Aarhus-C, Denmark.

⁸Department of Physics, Pennsylvania State University, University Park, Pennsylvania 16802, USA.

⁹Department of Physics and Beijing Key Laboratory of Opto-electronic Functional Materials & Micro-nano Devices, Renmin University of China, Beijing 100872, China.

¹⁰Research Center for Functional Materials, National Institute for Materials Science, 1-1 Namiki, Tsukuba 305-0044, Japan.

¹¹International Center for Materials Nanoarchitectonics, National Institute for Materials Science, 1-1 Namiki, Tsukuba 305-0044, Japan.

¹²Current address: Department of Physics, University of Science and Technology of China, Hefei, Anhui 230026, China.

*Corresponding author. Email: yongchen@purdue.edu

Abstract: Van der Waals (vdW) magnet heterostructures have emerged as new platforms to explore exotic magnetic orders and quantum phenomena. Here, we study heterostructures of layered antiferromagnets, CrI₃ and CrCl₃, with perpendicular and in-plane magnetic anisotropy, respectively. Using magneto-optical Kerr effect microscopy, we demonstrate out-of-plane magnetic order in the CrCl₃ layer proximal to CrI₃, with ferromagnetic interfacial coupling between the two. Such an interlayer exchange field leads to higher critical temperature than that of either CrI₃ or CrCl₃ alone. We further demonstrate significant electric-field control of the coercivity, attributed to the naturally broken structural inversion symmetry of the heterostructure allowing unprecedented direct coupling between electric field and interfacial magnetism. These findings illustrate the opportunity to explore exotic magnetic phases and engineer spintronic devices in vdW heterostructures.

Introduction

Heterostructures are promising to host emergent phenomena and device functions not present in constituent parts ¹⁻¹⁰. One well-known example is the integration of two insulating complex oxides leading to a conducting two-dimensional electron gas at the interface ², with surprising coexistence of superconductivity and ferromagnetism ³. The recently explored van der Waals (vdW) magnets have pushed the research frontier to 2D magnetism where exotic magnetic ground states and quantum phases can emerge ¹¹⁻¹⁸. Magnetic vdW heterostructures provide a new toolbox to explore magnetic proximity and related effects ⁴⁻¹⁰. A largely unexplored arena is to combine two different magnetic orders and investigate the magnetic proximity at the interface, which could allow modulation of magnetic interactions and establish exotic magnetic properties. It is also of fundamental significance to effectively control the exchange interactions and magnetic anisotropy, with the latter being crucial to stabilize the long-range magnetic orders.

The studies of layered semiconducting chromium trihalides have shown exotic magnetic behaviors and rich tunability by stimuli¹⁴⁻¹⁸. Typically, the few-layer CrI_3 is an antiferromagnet with Ising-like perpendicular magnetic anisotropy (PMA)^{19,20}, as schematically depicted in Fig. 1a. The interlayer antiferromagnetic coupling is ascribed to the exchange interactions between Cr mediated by ligand atoms^{17,20}. In contrast, few-layer CrCl_3 is an easy-plane antiferromagnet, where spins prefer to lie in the layers^{20,21}. In particular, the single-ion anisotropy from spin-orbit coupling (SOC) of Cr and the anisotropic exchange from SOC of Cl nearly cancel out each other^{20,21}. Therefore, CrCl_3 is located close to the boundary between PMA and in-plane anisotropy, suggesting that its magnetic properties may be particularly susceptible to external perturbations. The combined heterostructure of CrI_3 and CrCl_3 is possibly a fertile system to realize rich magnetic phases and manipulate them. Such a heterostructure has not yet been explored.

Here, we fabricate $\text{CrI}_3/\text{CrCl}_3$ heterostructures and demonstrate interfacial ferromagnetism between the two antiferromagnets. Figure 1a left panel schematically depicts the expected spin configurations for the magnetic ground states in bilayer (2L) CrI_3 and few-layer (FL) CrCl_3 with PMA and in-plane anisotropy¹⁹⁻²¹, respectively. Due to the strong intralayer ferromagnetic coupling in chromium trihalides¹⁷, we can denote all spins in a given layer by a macroscopic spin (out-of-plane: \uparrow, \downarrow ; in-plane: \leftarrow, \rightarrow). The optical micrograph of a representative 2L $\text{CrI}_3/\text{FL } \text{CrCl}_3$ heterostructure is shown in Fig. 1b. The 2L CrI_3 is partially stacked on top of FL CrCl_3 , allowing the comparison between regions of 2L CrI_3 , FL CrCl_3 and heterostructure. Atomic force microscopy confirms flake thickness of 1.6 nm for 2L CrI_3 (Fig. 1c) and 9.5 nm for FL CrCl_3 , respectively.

Results and Discussion

We employ magneto-optical Kerr effect microscopy (MOKE) under the polar configuration as the primary measurement due to its high sensitivity to the magnetic moments perpendicular to the sample surface²². Figure 1d shows the MOKE signal (θ_K) of the 2L CrI_3 and the 2L $\text{CrI}_3/\text{FL } \text{CrCl}_3$ heterostructure as a function of the perpendicular magnetic field. In the 2L CrI_3 region, θ_K stays close to zero at low field, corresponding to the antiferromagnetic states $\downarrow\uparrow$ or $\uparrow\downarrow$ with zero net magnetization. Beyond critical field ± 0.76 T, θ_K abruptly jumps to ferromagnetic states with finite magnetization. This is consistent with the reported spin-flip transitions in 2L CrI_3 ²³.

In the 2L CrI₃/FL CrCl₃ heterostructure, the antiferromagnetic-to-ferromagnetic spin-flip transition of 2L CrI₃ is still present and its critical field decreases from ± 0.76 T in 2L CrI₃ region to ± 0.57 T in the heterostructure region. Remarkably, a significant square hysteresis loop is observed with coercive field $\sim \pm 0.1$ T, indicating a magnetic transition between two different phases with non-zero net magnetization, in sharp contrast to the antiferromagnetic ground states in 2L CrI₃ ($\downarrow\uparrow$ or $\uparrow\downarrow$). Such a ferromagnetic-like loop is absent in either 2L CrI₃ or FL CrCl₃, suggesting its origin from interfacial magnetic interaction. This phenomenon should not be due to the charge transfer/doping-induced antiferromagnetic-to-ferromagnetic transition reported in 2L CrI₃^{14, 15}, which does not exhibit such a coexistence of antiferromagnetic-type and ferromagnetic-type transitions. Recent works have shown that a twist of two chromium trihalides layers may lead to noncollinear antiferromagnetic-ferromagnetic domains and thus finite MOKE signals^{9, 10, 18, 24}. However, this scenario is also less likely to be relevant, as such domains are predicted to emerge for sufficiently large moiré periodicity. Due to large lattice constant mismatch¹⁸, the CrI₃/CrCl₃ heterostructure can hardly form large moiré periodicity even at zero twist angle. Furthermore, the magnetization behaviors (including the field and temperature dependence) measured in twisted bilayer CrI₃^{9, 10} exhibit qualitative difference from what we observe in our samples. We further rule out several other possible origins (see detailed discussions in Supplementary Text 1). We propose that at least three spin layers (two layers of CrI₃ plus one neighboring layer of CrCl₃) are responsible for the observed transitions. The neighboring CrCl₃ layer is acting as the third spin layer with out-of-plane magnetic order after being stacked in proximity with CrI₃, as schematically shown in Fig. 1a and denoted in the red dashed rectangles in Fig. 1d,e. Note that a perpendicular magnetic field induces canting of the planar CrCl₃ spins, giving rise to a continuously varying MOKE background²⁵ (Supplementary Fig. 1), which is typically subtracted and eliminated from our MOKE signal. Therefore, only perpendicular spin-flip transitions are discussed in this work.

Similar to trilayer CrI₃, in principle several potential antiferromagnetic configurations can be considered: $\uparrow\downarrow\downarrow$ (-1), $\downarrow\uparrow\uparrow$ (+1), $\downarrow\uparrow\downarrow$ (-1), $\uparrow\downarrow\uparrow$ (+1) with the first two and the third spins referring to the 2L CrI₃ and the neighboring CrCl₃ layer respectively and the numbers in brackets denoting the net magnetic moments. To figure out the coupling type for the neighboring CrI₃ and CrCl₃ layers, we study the 1L CrI₃/FL CrCl₃ heterostructure where the magnetic behavior can directly verify the interlayer coupling type. Figure 1e shows θ_K of the 1L CrI₃ and the 1L CrI₃/FL CrCl₃ heterostructure, fabricated from the same CrI₃ flake. Interestingly, both show a ferromagnetic

behavior with a single hysteresis loop. This observation indicates that the neighboring CrI₃ and CrCl₃ layer is ferromagnetically coupled, in contrast to the interlayer antiferromagnetic coupling in FL CrI₃¹⁹. Careful inspection on the hysteresis loop in Fig. 1d shows more transition steps, possibly due to the switching of magnetic domains^{23, 26}. Note that due to thin-film optical interference effect^{23, 27}, it's not possible to associate the magnitude or sign of the MOKE signal to the magnetization of different samples (e.g., the doubling of the MOKE signal in the 1L CrI₃/FL CrCl₃ heterostructure relative to that in the 1L CrI₃ in Fig. 1e does not imply that the probed magnetization doubles). In the following text, we mainly focus on other features (e.g., emergent hysteresis loop, transition/coercive fields, critical temperatures). To exclude any unique causes related to the stacking sequence, we also studied reversely stacked heterostructures with FL CrCl₃ on top of 2L CrI₃ and observed similar hysteresis loops (Supplementary Figs. 2 and 3). The larger coercive field of the hysteresis loop observed in the reversed stack may be due to sample differences or twist angle dependence and is out of the scope of this work.

We next study the temperature dependence of the magnetism in the heterostructure. Figure 2a,b shows the temperature dependence of θ_K in 2L CrI₃ and 2L CrI₃/FL CrCl₃ heterostructure. The extracted H_1 , H_1^* , H_2^* and $\Delta\theta_1$, $\Delta\theta_1^*$, $\Delta\theta_2^*$ as a function of temperature are shown in Fig. 2c,d, respectively. The antiferromagnetic spin-flip transitions (at H_1 and H_1^*) in both 2L CrI₃ and the heterostructure disappear at temperatures larger than $T_C \sim 40$ K and is consistent with previous measurements in 2L CrI₃²⁸. The ferromagnetic-like hysteresis loop (at H_2^*) observed only in the heterostructure region survives up to a higher temperature $T_C^* \sim 48$ K. Another experiment on 1L CrI₃/FL CrCl₃ heterostructure shows critical temperatures of $T_C \sim 33$ K and $T_C^* \sim 37$ K for 1L CrI₃ region and heterostructure region, respectively (Supplementary Fig. 4). In 2D magnets, the critical temperature is determined by the spin-wave excitation gap, which is dictated by the anisotropies present in the system^{12, 23, 29, 30}. Our density functional theory (DFT) results suggest an increase in the effective single-ion anisotropy of CrI₃ when brought in proximity to CrCl₃. On the other hand, thanks to the induced ferromagnetic coupling, the CrCl₃ layer now sees an effective anisotropy field that depends both on the interfacial ferromagnetic coupling as well as the anisotropy of CrI₃, which is expected to enlarge the spin-wave gaps for both the materials. This is consistent with the observed increase of T_C for both 1L CrI₃/FL CrCl₃ and 2L CrI₃/FL CrCl₃ systems.

To better understand the observations, we explore the magnetic ground states of the CrI₃/CrCl₃ bilayer using first-principles calculations (Supplementary Text 2). We find that the perpendicular

ferromagnetic state ($\uparrow\uparrow$) is more favorable than three other magnetic configurations: perpendicular antiferromagnetic state ($\uparrow\downarrow$), the states that one layer is out-of-plane polarized while the other in-plane polarized ($\uparrow\rightarrow$ or $\rightarrow\uparrow$). Further consideration on magnetic dipole-dipole interaction and different commensurate twist angles (0° and 30°) does not undermine the favorable perpendicular ferromagnetic state. The interlayer exchange energy J_{inter} in $\text{CrI}_3/\text{CrCl}_3$ can be approximated by the energy difference between perpendicular antiferromagnetic and ferromagnetic configurations¹⁷. We estimate $J_{\text{inter}} \approx -77$ (-64) $\mu\text{J}/\text{m}^2$ for 0° (30°)-twisted $\text{CrI}_3/\text{CrCl}_3$, compared to the reported interlayer exchange ~ 80 $\mu\text{J}/\text{m}^2$ in 2L CrI_3 ^{29, 31, 32}. Such interfacial exchange coupling in the heterostructure wins over the in-plane anisotropy of CrCl_3 and results in the out-of-plane magnetic order in the CrCl_3 layer next to CrI_3 , in agreement with our observations.

We next turn to explore the electrical tunability of the observed interfacial magnetism. A unique aspect of the $\text{CrI}_3/\text{CrCl}_3$ heterostructure, when compared with previously explored monolayer and/or homobilayer systems^{14, 15, 33}, is the absence of structural inversion symmetry. The Neumann's principle³⁴ states that the spin-charge coupling is dictated by the symmetries of the system. We thus expect to observe spin-charge coupling phenomena for the interlayer magnetic order. In particular, breaking of structural inversion allows for direct electric-field modification of the magnetic anisotropy and the interlayer exchange interactions via terms of the form (see detailed discussions in Supplementary Text 3):

$$E_{\text{elec}}(\mathbf{m}_i, \sigma_i) = (\sigma_1 - \sigma_2)(\beta_1 m_{z1}^2 + \beta_2 m_{z2}^2 + \beta_3 \mathbf{m}_1 \cdot \mathbf{m}_2), \quad (1)$$

where \mathbf{m}_i , σ_i are the magnetization and charges of the respective layers, $(\sigma_1 - \sigma_2) \sim$ electric field and $\beta_{1,2,3}$ parameterizes the strength of respective interactions. Microscopically, the electric-field control of interfacial magnetic interactions could arise from electric-field-induced changes in the orbital occupancy in conjunction with spin-orbit interactions. Such a mechanism has attracted significant interest for constructing low-dissipation spintronic memory and logic devices^{35, 36}.

To check the electric-field tuning of the observed interfacial magnetism, we fabricated a dual-gated 1L $\text{CrI}_3/\text{FL CrCl}_3$ device, as shown in Fig. 3a,b. This structure allows us to study the magnetization of the $\text{CrI}_3/\text{CrCl}_3$ heterostructure (as well as that of the 1L CrI_3 region in the same device) under the top-gate voltage V_{tg} and back-gate voltage V_{bg} . The two voltages are converted to electrostatic doping density n and displacement field D (Methods). Figure 3c shows the coercive field (H_c) in 1L $\text{CrI}_3/\text{FL CrCl}_3$ heterostructure increases from ~ 700 Oe to ~ 1000 Oe when the D is

tuned from -1.4 V nm^{-1} to 1 V nm^{-1} , indicating the enhancement of the magnetic anisotropy of the interfacial ferromagnetism in the heterostructure. The full mappings in Fig. 3d,e present the extracted H_c as a function of both n and D in 1L CrI_3 and the 1L $\text{CrI}_3/\text{FL CrCl}_3$ heterostructure, respectively. A quite weak modulation of H_c is observed in 1L CrI_3 , suggesting that the magnetism of 1L CrI_3 can hardly be tuned under the range of gating voltages of this work. Separate experiments on FL CrCl_3 demonstrate that the magnetism of CrCl_3 also can hardly be tuned by electrostatic gating (Supplementary Fig. 5d). However, significant tunability of the H_c is observed by the D applied to the heterostructure. Such a dramatic tunability in the $\text{CrI}_3/\text{CrCl}_3$ is in agreement with the electric field control of interfacial magnetic interactions allowed by the structural symmetry breaking, predicted in the above theoretical analysis. The intriguing electrical tunability allowed by symmetry breaking is also observed in a heterostructure containing a bilayer CrI_3 (Supplementary Text 4).

In summary, we studied the interfacial magnetism in $\text{CrI}_3/\text{CrCl}_3$ heterostructures and demonstrated the interfacial ferromagnetic coupling between neighboring CrI_3 and CrCl_3 layers. The demonstrated ability to engineer magnetoelectric phenomena by breaking symmetries via vdW heterostructures provides opportunities for vdW spintronics. The compatible hybrids of 2D magnets with other quantum materials, such as unconventional superconductors, ferroelectrics or topological materials are predicted to demonstrate exotic topological phases and many-body interactions^{12, 13, 37}, as well as to design new spintronic devices and therefore are highly desirable for further study.

Methods

Crystal growth. Single crystal CrI_3 was synthesized using the chemical vapor transport (CVT) method³⁸. The Cr powder and iodine pieces were mixed with a stoichiometric ratio and loaded into a quartz tube (inner diameter, 10 mm; length, 180 mm). The quartz tube was sealed under vacuum and then transferred to a double temperature zones furnace. The temperatures of the hot and cold ends of the furnace were set at 650°C and 550°C , respectively. The growth with such a temperature gradient lasted for 7 days. Finally, the furnace was shut down, and the quartz tube naturally cooled down to room temperature. The black plate-like CrI_3 crystals can be found at the cold end of the quartz tube.

Single crystal CrCl_3 was grown by the CVT method. The commercial CrCl_3 polycrystal powder (99.9%) was sealed in a silica tube with a length of 200 mm and an inner diameter of 14 mm. The tube was pumped down to 0.01 Pa and sealed under vacuum, and then placed in a two-zone horizontal tube furnace. The two growth zones were raised slowly to 973 K and 823 K for 2 days, and then held there for another 7 days. After that, the furnace was shut down and cooled down naturally. Shiny, plate-like crystals with lateral dimensions of up to several millimeters can be obtained from the growth.

Device fabrication. Few-layer CrI_3 , CrCl_3 and hexagonal boron nitride (hBN) flakes are exfoliated onto the silicon wafer covered by 285-nm thermal oxide layer. Flakes with proper thickness are selected by optical contrast²³ and later confirmed by atomic force microscopy (AFM) and MOKE measurements. CrI_3 flakes used in this work have 1~2 layers and the few-layer CrCl_3 flakes are around 5~10 nm (0.6 nm for each layer) thick. Heterostructures of CrI_3 and CrCl_3 are fabricated by the dry-transfer method and encapsulated between two hBN flakes with a typical thickness of ~10 nm. Specifically, a stamp made of a thin polycarbonate and polydimethylsiloxane is then employed to pick up the flakes in sequence under an optical microscope. In the end, the finished stack is deposited onto the target substrate with polycarbonate on top which is removed by chloroform afterwards. The whole process is performed inside a glovebox to avoid material degradation. The exposure time to air is kept below ten minutes before transferring the fabricated sample into the measurement chamber and pumping down.

For the dual-gated heterostructure device and magnetic tunneling junction device, few-layer graphene flakes are exfoliated and integrated into the stack following the above processes. The target substrate is pre-patterned with electrodes fabricated by standard e-beam lithography, Au/Ti deposition and lift-off processes. The stack is carefully aligned and transferred onto the target pattern to make contact between graphene flakes and electrodes.

MOKE microscopy. The polarization of a linearly polarized light reflected from a magnetic material will be rotated by a Kerr angle θ_K , which is proportional to the magnetization of the material. In this work, the incident light is normal to the sample plane and MOKE is in the polar geometry, meaning that the magnetic vector being probed is perpendicular to the sample surface and parallel to the incident light. A balanced photodetector and lock-in method are used to obtain the MOKE signal. A laser is used here with wavelength of 633 nm and power of 5 μW . The sample

is placed in a helium-flow optical cryostat with the temperature down to 6 K and magnetic field (perpendicular to sample surface) up to 5 T. The laser is focused onto the sample surface by an objective with the spot diameter of 0.5 μm .

Electrical control of the dual-gated device. Top-gate and back-gate voltages can be applied to the few-layer graphene gates in the heterostructure device, while the graphene contact to the heterostructure is grounded. The dual-gate structure allows independent control of the doping density and displacement field applied on the heterostructure. The doping density n and displacement field D are extracted by the simple parallel plate capacitor model. For simplicity, the $\text{CrI}_3/\text{CrCl}_3$ heterostructure is regarded as one channel, on which the doping density and electric field are applied. The quantum capacitance of CrI_3 and CrCl_3 is much larger than that of graphene due to the nearly flat bands of these two magnetic semiconductors¹⁵. Therefore, only geometric capacitances C_{bg} and C_{tg} are considered. The doping density and displacement field can be written as $n = C_{\text{bg}} \cdot V_{\text{bg}} + C_{\text{tg}} \cdot V_{\text{tg}}$ and $D = (D_{\text{bg}} + D_{\text{tg}})/2 = (\epsilon_{\text{bg}} \cdot V_{\text{bg}}/d_{\text{bg}} - \epsilon_{\text{tg}} \cdot V_{\text{tg}}/d_{\text{tg}})/2$, respectively. The relative dielectric constant of hBN¹⁴ is $\epsilon_{\text{bg}} = \epsilon_{\text{tg}} = 3$. For the device in Fig. 3, the thicknesses of bottom hBN and top hBN are obtained by AFM measurement to be $d_{\text{bg}} = 19.6$ nm and $d_{\text{tg}} = 14.9$ nm, respectively.

Data and code availability. The data and code supporting the findings of this study are included in the paper and its Supplementary Information file. Further data and code sets are available from the corresponding author on reasonable request.

References

1. Geim, A. K. & Grigorieva, I. V. Van der Waals heterostructures. *Nature* **499**, 419-425 (2013).
2. Ohtomo, A. & Hwang, H. Y. A high-mobility electron gas at the $\text{LaAlO}_3/\text{SrTiO}_3$ heterointerface. *Nature* **427**, 423-426 (2004).
3. Bert, J. A., *et al.* Direct imaging of the coexistence of ferromagnetism and superconductivity at the $\text{LaAlO}_3/\text{SrTiO}_3$ interface. *Nat. Phys.* **7**, 767-771 (2011).
4. Zhong, D., *et al.* Van der Waals engineering of ferromagnetic semiconductor heterostructures for spin and valleytronics. *Sci. Adv.* **3**, e1603113 (2017).
5. Fu, H. X., Liu, C. X. & Yan, B. H. Exchange bias and quantum anomalous Hall effect in the $\text{MnBi}_2\text{Te}_4/\text{CrI}_3$ heterostructure. *Sci. Adv.* **6**, eaaz0948 (2020).
6. Kezilebieke, S., *et al.* Topological superconductivity in a van der Waals heterostructure. *Nature* **588**, 424-428 (2020).
7. Tong, Q. J., Liu, F., Xiao, J. & Yao, W. Skyrmions in the moiré of van der Waals 2D magnets. *Nano Lett.* **18**, 7194-7199 (2018).
8. Hejazi, K., Luo, Z.-X. & Balents, L. Heterobilayer moiré magnets: Moiré skyrmions and commensurate-incommensurate transitions. *Phys. Rev. B* **104**, L100406 (2021).
9. Song, T., *et al.* Direct visualization of magnetic domains and moiré magnetism in twisted 2D magnets. *Science* **374**, 1140-1144 (2021).
10. Xu, Y., *et al.* Coexisting ferromagnetic–antiferromagnetic state in twisted bilayer CrI_3 . *Nat. Nanotechnol.* **17**, 143-147 (2021).
11. Fei, Z. Y., *et al.* Two-dimensional itinerant ferromagnetism in atomically thin Fe_3GeTe_2 . *Nat. Mater.* **17**, 778-782 (2018).
12. Gibertini, M., Koperski, M., Morpurgo, A. F. & Novoselov, K. S. Magnetic 2D materials and heterostructures. *Nat. Nanotechnol.* **14**, 408-419 (2019).
13. Burch, K. S., Mandrus, D. & Park, J. G. Magnetism in two-dimensional van der Waals materials. *Nature* **563**, 47-52 (2018).
14. Huang, B., *et al.* Electrical control of 2D magnetism in bilayer CrI_3 . *Nat. Nanotechnol.* **13**, 544-548 (2018).
15. Jiang, S. W., Li, L. Z., Wang, Z. F., Mak, K. F. & Shan, J. Controlling magnetism in 2D CrI_3 by electrostatic doping. *Nat. Nanotechnol.* **13**, 549-553 (2018).
16. Li, T. X., *et al.* Pressure-controlled interlayer magnetism in atomically thin CrI_3 . *Nat. Mater.* **18**, 1303-1308 (2019).
17. Sivadas, N., Okamoto, S., Xu, X. D., Fennie, C. J. & Xiao, D. Stacking-dependent magnetism in bilayer CrI_3 . *Nano Lett.* **18**, 7658-7664 (2018).
18. Akram, M., LaBollita, H., Dey, D., Kapeghian, J., Erten, O. & Botana, A. S. Moiré skyrmions and chiral magnetic phases in twisted CrX_3 ($X = \text{I, Br, and Cl}$) bilayers. *Nano Lett.* **21**, 6633-6639 (2021).
19. Song, T. C., *et al.* Giant tunneling magnetoresistance in spin-filter van der Waals heterostructures. *Science* **360**, 1214-1218 (2018).
20. Tartaglia, T. A., *et al.* Accessing new magnetic regimes by tuning the ligand spin-orbit coupling in van der Waals magnets. *Sci. Adv.* **6**, eabb9379 (2020).
21. Wang, Z., *et al.* Determining the phase diagram of atomically thin layered antiferromagnet CrCl_3 . *Nat. Nanotechnol.* **14**, 1116-1122 (2019).
22. Wu, M., Li, Z. L., Cao, T. & Louie, S. G. Physical origin of giant excitonic and magneto-optical responses in two-dimensional ferromagnetic insulators. *Nat. Commun.* **10**, 2371 (2019).
23. Huang, B., *et al.* Layer-dependent ferromagnetism in a van der Waals crystal down to the monolayer limit. *Nature* **546**, 270-273 (2017).
24. Hejazi, K., Luo, Z. X. & Balents, L. Noncollinear phases in moiré magnets. *Proc. Natl. Acad. Sci. U.S.A.* **117**, 10721-10726 (2020).

25. Cai, X. H., *et al.* Atomically thin CrCl₃: an in-plane layered antiferromagnetic insulator. *Nano Lett.* **19**, 3993-3998 (2019).
26. Sun, Q. C., *et al.* Magnetic domains and domain wall pinning in atomically thin CrBr₃ revealed by nanoscale imaging. *Nat. Commun.* **12**, 1989 (2021).
27. Ma, Z. W., *et al.* Micro-MOKE with optical interference in the study of 2D Cr₂Ge₂Te₆ nanoflake based magnetic heterostructures. *AIP Adv.* **9**, 125116 (2019).
28. Jiang, S. W., Shan, J. & Mak, K. F. Electric-field switching of two-dimensional van der Waals magnets. *Nat. Mater.* **17**, 406-410 (2018).
29. Lu, X., Fei, R. & Yang, L. Curie temperature of emerging two-dimensional magnetic structures. *Phys. Rev. B* **100**, 205409 (2019).
30. Gong, C., *et al.* Discovery of intrinsic ferromagnetism in two-dimensional van der Waals crystals. *Nature* **546**, 265-269 (2017).
31. Lado, J. L. & Fernández-Rossier, J. On the origin of magnetic anisotropy in two dimensional CrI₃. *2D Mater.* **4**, 035002 (2017).
32. Cenker, J., *et al.* Direct observation of two-dimensional magnons in atomically thin CrI₃. *Nat. Phys.* **17**, 20-25 (2021).
33. Rustagi, A., Solanki, A. B., Tserkovnyak, Y. & Upadhyaya, P. Coupled spin-charge dynamics in magnetic van der Waals heterostructures. *Phys. Rev. B* **102**, 094421 (2020).
34. Birss, R. R. *Symmetry and Magnetism* (North-Holland, Amsterdam, 1966).
35. Baek, S. H. C., *et al.* Complementary logic operation based on electric-field controlled spin-orbit torques. *Nat. Electron.* **1**, 398-403 (2018).
36. Lee, H., Ebrahimi, F., Amiri, P. K. & Wang, K. L. Low-power, high-density spintronic programmable logic with voltage-gated spin Hall effect in magnetic tunnel junctions. *IEEE Magn. Lett.* **7**, 3102505 (2016).
37. Kezilebieke, S., *et al.* Topological superconductivity in a van der Waals heterostructure. *Nature* **588**, 424-428 (2020).
38. Liu, Y. & Petrovic, C. Three-dimensional magnetic critical behavior in CrI₃. *Phys. Rev. B* **97**, 014420 (2018).

Acknowledgements

We thank Di Xiao, Wenguang Zhu for helpful discussions and Adam W. Tsen for help with crystals. The first-principles calculations have been done on the supercomputing system in the Supercomputing Center of the University of Science and Technology of China. **Funding:** We acknowledge partial support of the work from WPI-AIMR, JSPS KAKENHI Basic Science A (18H03858), New Science (18H04473 and 20H04623), Tohoku University FRiD program, Department of Defense (DOD) Multidisciplinary University Research Initiatives (MURI) program (FA9550-20-1-0322), US Department of Energy (DOE) Office of Science through the Quantum Science Center (QSC, a National Quantum Information Science Research Center), and Villum Foundation. Z.Q.M. acknowledges the support by the US DOE under grants DE-SC0019068 for sample synthesis. H.C.L. acknowledges the support by National Key R&D Program of China (2018YFE0202600), Beijing Natural Science Foundation (Z2000005), and National Natural

Science Foundation of China (11822412 and 11774423). K.W. and T.T. acknowledge support from the Elemental Strategy Initiative conducted by the MEXT, Japan (JPMXP0112101001) and JSPS KAKENHI (19H05790, 20H00354 and 21H05233).

Author contributions

G.H.C. and Y.P.C. conceived the project. G.H.C. fabricated the devices and performed experiments, assisted by A.L.A. M.M.R., Z.P.H., A.R., K.A.S. and P.U. performed supporting theoretical modeling. Y.L.Z. and Z.Q.M. provided bulk CrI_3 crystals. S.H.Y, S.J.T. and H.C.L. provided bulk CrCl_3 crystals. K.W. and T.T. provided bulk hBN crystals. Y.P.C. supervised the project. G.H.C., M.M.R., Z.P.H., P.U. and Y.P.C. wrote the manuscript with input from all authors.

Competing interests

The authors declare no competing interests.

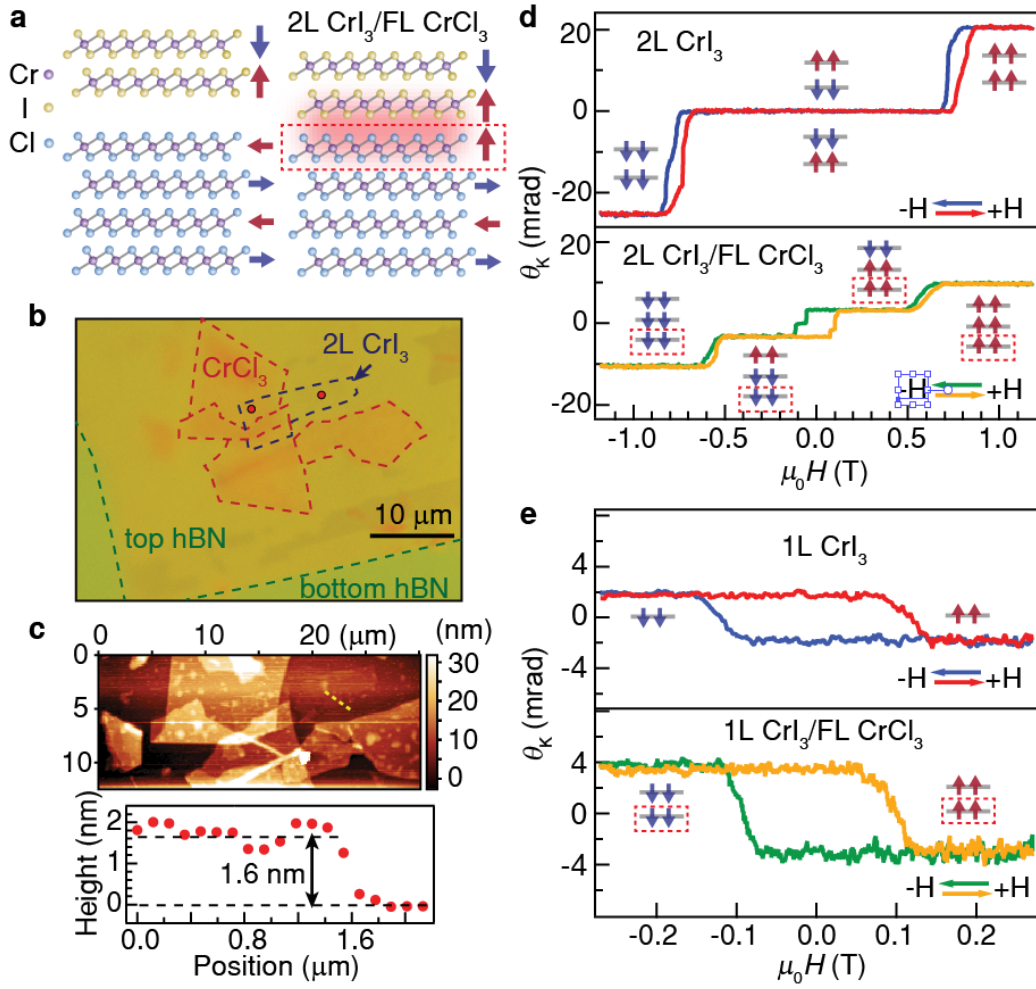


Figure 1 | CrI₃/CrCl₃ heterostructures and MOKE measurements. **a**, Schematics of the magnetic ground states in bilayer (2L) CrI₃ and few-layer (FL) CrCl₃ before (left) and after (right) forming heterostructure. Only four layers of CrCl₃ are shown for simplicity. **b**, Optical micrograph of a 2L CrI₃/FL CrCl₃ heterostructure. **c**, Atomic force microscopy of the heterostructure in the same position as in **b**. The height profile (along the yellow dotted line in the image) at the edge of CrI₃ indicates the thickness of a bilayer. **d**, MOKE signal (after subtracting a polynomial background, as done for all MOKE curves in the main text) of the 2L CrI₃ region and the 2L CrI₃/FL CrCl₃ heterostructure region as a function of perpendicular magnetic field. Two curves of each region represent forward and backward sweeps of the field, respectively. The data is taken at the spots marked by red in **b**. Insets depict magnetic ground states of 2L CrI₃ and the CrI₃/CrCl₃ heterostructure (showing only the interfacial CrCl₃ layer, highlighted by red dashed rectangles). **e**, MOKE signal of another monolayer (1L) CrI₃/FL CrCl₃ heterostructure, compared with that measured in the 1L CrI₃ (from the same CrI₃ flake as in the heterostructure region).

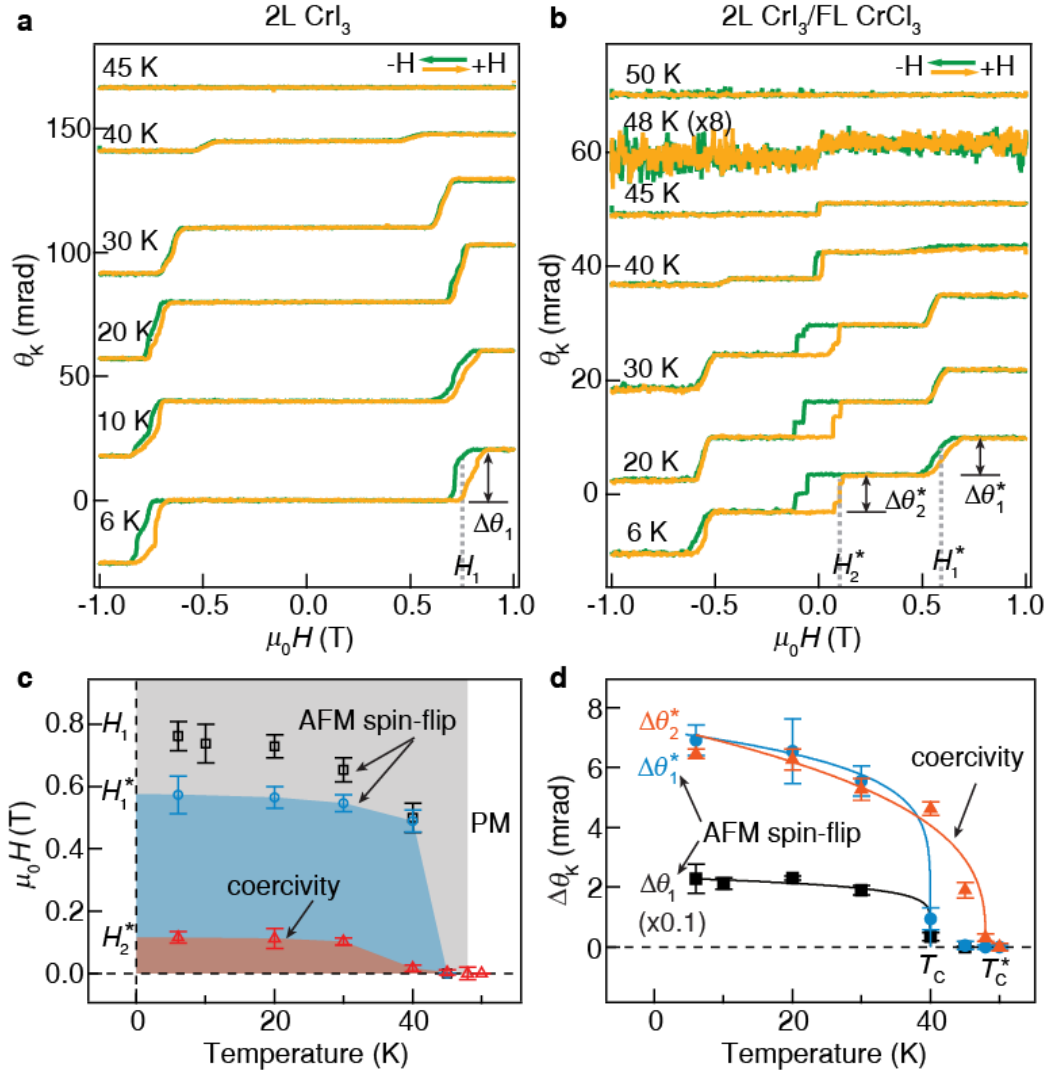


Figure 2 | Temperature dependence of the magnetism of 2L CrI₃ and 2L CrI₃/FL CrCl₃ heterostructure. **a,b**, MOKE signal in the 2L CrI₃ region (**a**) and the 2L CrI₃/FL CrCl₃ heterostructure region (**b**) as a function of perpendicular magnetic field at different temperatures. Critical fields H_1 , H_1^* , H_2^* and magnitudes in the change of MOKE signal $\Delta\theta_1$, $\Delta\theta_1^*$, $\Delta\theta_2^*$ of magnetic transitions are labeled. **c**, Temperature dependence of the critical fields of magnetic transitions. PM: paramagnetic. The critical fields are extracted from the peak of derivative $d\theta_k/dH$ and the error bars are the peak widths. **d**, Temperature dependence of the magnitudes in the change of MOKE signal at magnetic transitions. Solid curves are fitted by a power-law equation ¹¹. The critical temperatures T_c and T_c^* are indicated. The error bars are the uncertainties in extracting the transition magnitudes.

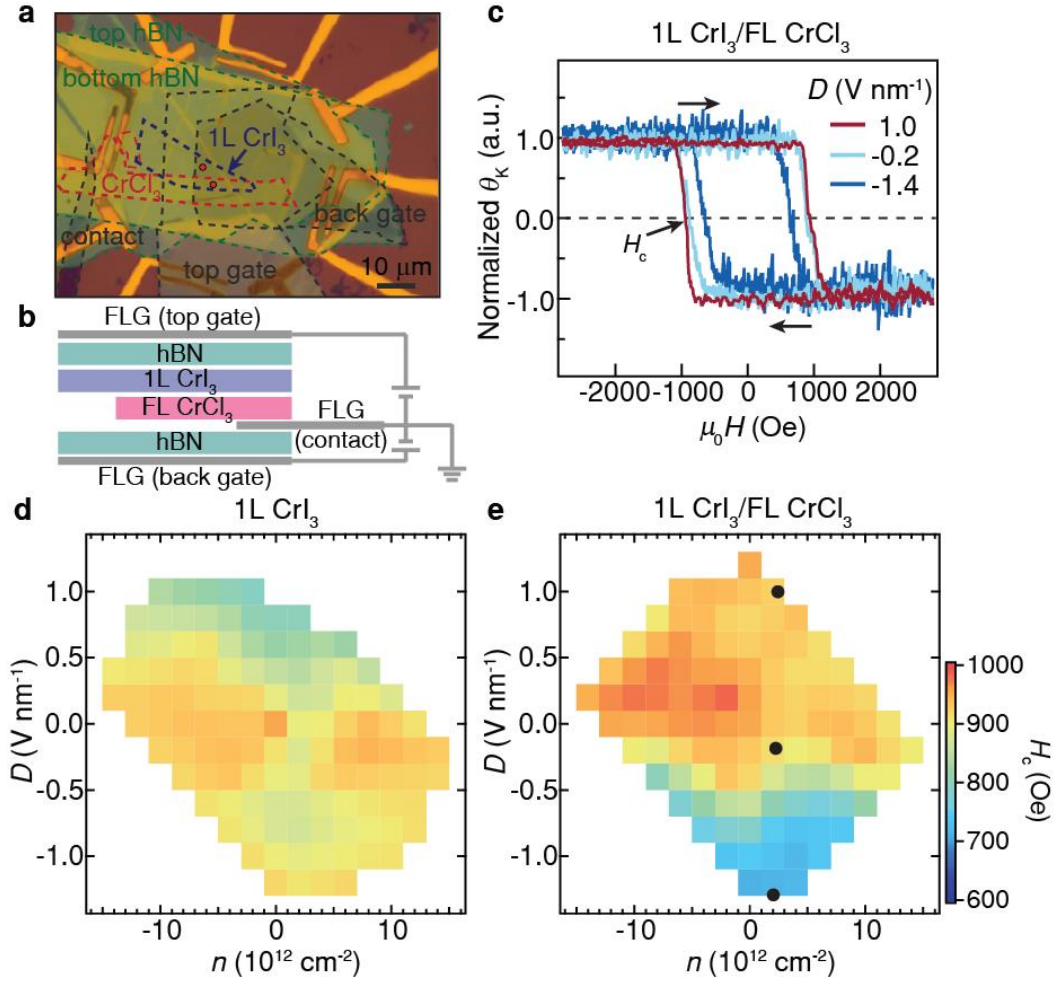


Figure 3 | Electrical control of the magnetism in 1L CrI₃/FL CrCl₃ heterostructure. **a,b**, Optical micrograph and schematic structure of a dual-gated 1L CrI₃/FL CrCl₃ device. Three few-layer graphene (FLG) flakes are used as back/top gates and the contact to the stack. **c**, Normalized MOKE signal as a function of perpendicular magnetic field in 1L CrI₃/FL CrCl₃ heterostructure under different displacement fields $D = -1.4, -0.2, 1.0$ V nm⁻¹. **d,e**, Coercive field H_c as a function of electrostatic doping density n and displacement field D of 1L CrI₃ (**d**) and 1L CrI₃/FL CrCl₃ heterostructure (**e**), respectively. The black dots in **e** correspond to the MOKE curves in **c**. The data is taken at the spots marked by red in **a**.